# Single-molecule FRET-tracking of InlB-activated MET receptors in living cells

Yunqing Li[1], Marina S. Dietz[1], Hans-Dieter Barth[1], Hartmut H. Niemann[2], Mike Heilemann[1,#]

[1]Institute of Physical and Theoretical Chemistry, Goethe-University Frankfurt, Max-von-Laue-Strasse 7, 60438 Frankfurt, Germany
[2]Department of Chemistry, Bielefeld University, Universitaetsstrasse 25, 33615 Bielefeld, Germany

[#]Corresponding authors, contact: heilemann@chemie.uni-frankfurt.de

## Abstract

The activation of transmembrane receptors through the binding of external ligands initiates information transfer across the cell membrane. Understanding these processes requires observations in living cells. Given the heterogeneity and lack of synchronization of such events demands for single-molecule experiments that can resolve distinct sub-populations. Here, we combine single-molecule FRET microscopy and single-particle tracking to track the ligand-induced dimerization and activation of the MET receptor tyrosine kinase in the plasma membrane of living cells. First, using fluorophore-labeled variants of the MET ligand internalin B (InlB), we determined the lifetime of a ligand-activated dimeric $(MET:InlB)_2$ receptor complex to around 1 second. Next, we determined the diffusion coefficient from monomeric and dimeric MET:InlB complexes from single-molecule FRET trajectories and found an about 1.6-fold slower diffusion of the dimeric receptor as compared to the monomeric receptor, accompanied by spatially restricted motion. The combination of single-molecule FRET and single-particle tracking delivers essential biophysical parameters of membrane receptor activation in living cells.

## Keywords

MET, receptor tyrosine kinase, single-molecule FRET, single-particle tracking, live-cell microscopy

## Introduction

The transmembrane receptor MET, also known as hepatocyte growth factor receptor (HGFR), belongs to the class of receptor tyrosine kinases (RTKs) and plays a central role in regulating key cellular functions, including proliferation, migration, morphogenesis, and tissue regeneration [1–3]. Dysregulation of MET is associated with various diseases, including cancer [4–6]. MET is activated upon binding of its physiological ligand, hepatocyte growth factor/scatter factor (HGF/SF) [7, 8], its natural isoform NK1 [9, 10], and the bacterial ligand InlB [11, 12]. Ligand binding promotes the formation of a 2:2 complex, consisting of two MET receptors and two ligands, which promotes cross-phosphorylation of MET within the complex and the subsequent initiation of downstream signaling cascades [13]. MET signaling is regulated by receptor internalization and degradation [14–16].

InlB plays a critical role in bacterial pathogenesis by exploiting host cell signaling machinery to facilitate bacterial entry [12, 17, 18]. *Listeria monocytogenes*, a Gram-positive pathogen responsible for listeriosis, expresses InlB on its surface to mediate invasion into nonphagocytic cells [19]. Through high-affinity interaction with MET, InlB hijacks host signaling pathways that ultimately support bacterial internalization and systemic infection [12, 20–23]. Therefore, a complete understanding of the dynamics and mechanisms of MET activation via InlB is important. The activity and structure of the MET:InlB dimer were studied in detail with x-ray crystallography, biochemical tools, single-molecule microscopy, and molecular dynamics simulation [24–29]. However, until now, the dynamics of the MET:InlB dimer were only studied indirectly using single-particle tracking [25, 30], whereas information on the stability, i.e., lifetime, of the $(MET:InlB)_2$ dimer was so far inaccessible

The lifetime of ligand-induced RTK dimers is a key determinant of signaling duration before receptor internalization or dissociation. This lifetime is regulated by interactions with ligands, co-receptors, other cellular structures (lipids, actin cytoskeleton), and downstream signaling proteins [31–36]. The stability of the dimer influences the recruitment of adaptor proteins to the phosphorylated intracellular tyrosine residues generated upon dimerization, thereby modulating downstream signaling pathways [16, 37]. For example, prolonged dimerization of EGFR has been shown to enhance proliferative signaling [38, 39]. Consequently, measuring both the lifetime and diffusion properties of RTK dimers in living cells is key information to describe receptor activation kinetics and spatial dynamics within the native membrane environment. It also serves as a reference measure for the development of drugs that aim to destabilize receptor dimers or weaken receptor activation in a disease context. Because of the technical complexity of accessing this information in living cells, comprehensive studies of these parameters simultaneously remain exceedingly rare.

In this study, we determine the diffusion dynamics of InlB-bound MET monomers and dimers in living cells by combining single-molecule Förster resonance energy transfer (smFRET) and single-particle tracking (SPT). In addition, we measure the dimer lifetime and lateral mobility of MET receptors in the plasma membrane. Our results provide quantitative information on the stability and dynamics of MET:InlB dimers, complementing the biophysical model of receptor activation.

## Material and methods

### *Passivation of coverslips with PLL-PEG-RGD*

Glass surfaces were passivated with RGD-grafted poly-L-lysine-graft-(polyethylene glycol) (PLL-PEG-RGD) to simultaneously minimize nonspecific binding and promote cell attachment. For live-cell measurements, coverslips were sonicated in isopropanol for 20 min at 35 °C using an ultrasonic bath (S30H Elmasonic, Elma electronic GmbH, Germany). They were then rinsed three times with deionized water ($ddH_2O$) and dried with nitrogen gas. Plasma cleaning was performed for 10 min using nitrogen at 80% power and approximately 0.3 mbar pressure. A 10 µL aliquot of 0.8 mg/mL PLL-PEG-RGD solution was applied between two coverslips and incubated for 1.5 h at room temperature in a 10 cm culture dish. After incubation, coverslips were gently separated, rinsed with $ddH_2O$, dried under nitrogen, and transferred to 6-well plates. Coverslips were stored under argon, sealed with Parafilm, and kept at −20 °C for up to two weeks before use [30]. For fixed cell measurements, 8-well chambers (SARSTEDT AG & Co. KG, Nümbrecht, Germany) were passivated with PLL-PEG-RGD according to Li et al. [29].

### *Cell culture*

The human osteosarcoma cell line U-2 OS (CLS Cell Lines Service GmbH, Eppelheim, Germany) was cultivated in high glucose Dulbecco's modified Eagle medium/nutrient mixture F-12 (DMEM/F12, Gibco, Life Technologies, Waltham, MA, USA), supplemented with 1% GlutaMAX (Gibco, Life Technologies) and 10% fetal bovine serum (FBS) (Gibco, Life Technologies) at 37 °C with 5% $CO_2$ in an automatic $CO_2$ incubator (Model C 150, Binder GmbH, Tuttlingen, Germany) and passaged every 3 to 4 days.

For live cell imaging experiments, 2 mL of a suspension containing $3 \times 10^4$ U-2 OS cells in complete growth medium supplemented with 1 unit/mL penicillin and 1 µg/mL streptomycin (Gibco, Life Technologies) was seeded per well in a 6-well plate (Greiner, Bio-One International GmbH, Kremsmünster, Österreich), which has been supplemented with PLL-PEG-RGD-coated glass coverslips with a diameter of 25 mm (VWR International GmbH). Cells were allowed to adhere and grow for three days prior to measurement.

For smFRET in fixed cells, U-2 OS cells were seeded in 8-well chambers (SARSTEDT AG & Co. KG, Nümbrecht, Germany) passivated with PLL-PEG-RGD. 300 µL cell suspension per well with $1.5 \times 10^4$

cells supplemented with 1 unit/mL penicillin and 1 µg/mL streptomycin (Gibco, Life Technologies) were seeded for 2 to 3 days to adhere and grow before measurement.

*Sample preparation*

For ligand stimulation, H and T cysteine variants (K64C, K280C) of InlB were site-specifically labeled with Cy3B and ATTO 647N using maleimide chemistry for thiol-specific labeling, as previously described [29].

Prior to live-cell imaging, coverslips with U-2 OS cells were mounted into custom-built holders, and 500 µL of pre-warmed live-cell imaging solution (Gibco) was added. Cells were incubated at room temperature for 10 min to reduce temperature-induced variability. Afterward, an oxygen scavenging buffer was added, consisting of 0.009 U/µL glucose oxidase from *Aspergillus niger* (Type VII), 594 U/mL catalase from bovine liver, 0.083 M glucose, and 1 mM Trolox (all from Sigma-Aldrich, St. Louis, MO, USA). 30 nM of each Cy3B- and ATTO 647N-labeled $InlB_{321}$ variants (T-T or H-T) were added to ensure stoichiometric labeling of MET by InlB. The InlB-containing buffer was incubated with the cells for 5 min before the measurement.

Fixed-cell smFRET experiments were performed as previously described [29]. Briefly, cells were incubated with 5 nM of each $InlB_{321}$ variant for 15 min at 37 °C and subsequently fixed for 15 min with 4% formaldehyde (Thermo Scientific) and 0.01% glutaraldehyde (Sigma-Aldrich) in 0.4 M sucrose and 1× PBS. For measurements, a freshly prepared oxygen-scavenging buffer (see above) was added.

*smFRET acquisition*

Single-molecule imaging was performed using a custom-built TIRF microscope. Cells were measured at room temperature for 30 min. Two lasers, 637 nm (140 mW OBIS) and 561 nm (200 mW Sapphire) from Coherent Inc. (Santa Clara, CA, USA), were used for excitation. The laser beams were collinearly aligned via a dichroic mirror (H 568 LPXR superflat, AHF Analysentechnik AG, Tübingen, Germany) and modulated through an acousto-optical tunable filter (AOTF; AOTFnC-400.650-TN, AA Opto-Electronic, Orsay, France), which allowed for rapid alternating excitation. The switching frequency of the laser excitation was regulated by two digital counters and analog output boards (NI PCI-6602 and NI PCI-6713, National Instruments, Austin, TX, USA). After passing through the AOTF, the laser beams were coupled into a single-mode optical fiber (P5-460AR-2, Thorlabs) via a fiber collimator (PAF-X-7-A, Thorlabs, Dachau, Germany) and re-collimated to a 2 mm beam diameter upon exiting the fiber using a collimation unit (60FC-0-RGBV11-47, Schäfter & Kirchhoff, Hamburg, Germany). The collimated beams were directed onto a dual-axis galvo mirror system (GVS012/M, Thorlabs), which enabled precise control of the illumination mode between wide-field, stationary TIRF, circular TIRF, or highly inclined laminated optical sheet (HILO) illumination via a custom, Python-based control script. The excitation light was delivered into an inverted microscope (IX-71, Olympus Deutschland GmbH, Hamburg, Germany) and focused onto the back focal plane of the objective (UPlanXApo, 100x, NA 1.45, Olympus Deutschland GmbH) using a pair of telescope lenses (AC255-050-A-ML and AC508-100-A-ML, Thorlabs). Excitation and emission paths were spectrally filtered by a set of optical filters and dichroic mirrors (Dual Line Clean-up ZET561/640x, Dual Line rejection band ZET 561/640, Dual Line beam splitter zt561/640rpc, AHF Analysentechnik AG). Z-axis stability during acquisition was maintained using a nosepiece stage (IX2-NPS, Olympus Deutschland GmbH), minimizing focus drift over time. Fluorescence emission was collected by the same objective and directed to the detection pathway via the dichroic mirror. For dual-color imaging, an image splitter (Optosplit II, Cairn Research Ltd, UK) was employed, equipped with a beam splitter and two bandpass filters (H643 LPXR, 590/20 BrightLine HC, 679/41 BrightLine HC, AHF Analysentechnik AG). Both emission channels were recorded simultaneously on an EMCCD camera

(iXon Ultra X-10971, Andor Technology Ltd, Belfast, UK), yielding a final optical magnification of 100× and an effective pixel size of 159 nm.

The live-cell measurements followed the smFRET recovery after photobleaching (smFRET-RAP) method [40]. Specifically, the overlapping signals from the basal membrane of the cells were first photobleached 5 to 10 min using 561 nm (67.7 W/cm$^2$) and 637 nm (552.1 W/cm$^2$) laser illumination in TIRF mode. After allowing signal recovery from the apical and lateral membranes for 1 min without illumination, 4000 frames were acquired using 561 nm excitation (19.8 W/cm$^2$ ) for FRET observation. Control measurements consisting of 500 frames were acquired before and after the photobleaching process to assess photobleaching and signal recovery, using 561 nm (19.8 W/cm$^2$) and 637 nm (76.5 W/cm$^2$) laser excitation. A transmitted light image was recorded after each measurement to confirm cell integrity. The acquisition was controlled using the μManager software [41], using 40 ms integration time, 200 EM gain, 3 times preamp gain, 17 MHz readout rate, and activated frame transfer for a region of interest (ROI) of 512 × 256 px. For channel alignment, 100-frame image sequences of 100 nm TetraSpeck™ microspheres were acquired using 561 nm and 637 nm laser excitation at the start of each measurement day.

For smFRET measurements in fixed cells with alternating laser excitation, 1000 frames were acquired with an exposure time of 100 ms, activated frame transfer, an EM gain of 150, a preamp gain of 3x, a readout rate of 17 MHz, and an image size of 512 x 256 pixels. A transmitted light image was taken per measurement. The excitation lasers (561 nm: 47 W/cm$^2$, 637 nm: 172 W/cm$^2$) were alternated with a frequency of 10 Hz.

*Data analysis*

The recorded field of view was separated into donor and acceptor channels using ROIs identified from 100 nm TetraSpeck™ calibration measurements in iSMS [42], applying the autoalign ROIs tool with default settings. The donor and acceptor channels were then tracked separately using u-track [43] with the following parameters: localization using Gaussian Mixture-model fitting with data-driven PSF radius derived in 10 iterations, 2D tracking with 3 frames gap closure time and 20 frames as the minimum length of a trajectory. The trajectories detected by u-track were further processed using the smCellFRET software [40] to identify those smFRET trajectories that showed either an increase in donor intensity upon disappearance of the acceptor or a decrease in donor intensity upon an increase in acceptor intensity. The donor trajectory is concatenated with the nearest matching donor trajectory within a 250 nm search radius at the position where the acceptor signal disappeared. After selecting the smFRET trajectories, the FRET intensity traces were summarized and exported using SPARTAN [44]. The FRET efficiency was calculated based on the equations introduced by Li et. al. [29].

Besides the intensities of donor and acceptor, the coordinates of smFRET trajectories were extracted using custom Matlab and Python scripts. Each trajectory was segmented into two parts: the fraction that is FRET-active and the donor-only fraction following the disappearance of the acceptor signal. The assignment process consisted of 3 steps: (1) Repeated localizations at the same position of donor and acceptor channels were merged to one localization; (2) Donor coordinates that spatially overlapped with the coordinates of the acceptor were identified as part of the FRET trajectory; (3) Donor coordinates with no matching acceptor signal were assigned to the donor-only trajectory segment. Trajectory characteristics, including diffusion coefficients determined by a global mean squared displacement (MSD) fit for the first four displacement points, dynamic localization precision, and type of motion, were extracted from the MSD plot according to the description in Harwardt et. al. [30]. The lifetimes of the FRET trajectories were collected by analyzing the length of the FRET traces. Visualization of the results was done using OriginPro (version 2023, OriginLab Corporation, Northampton, MA, USA).

smFRET measurements in fixed cells were analyzed with iSMS. smFRET data were deposited in the EMBL BioImaging Archive (https://www.ebi.ac.uk/biostudies/bioimages/studies/S-BIAD1347).

## Results

*smFRET of (MET:InlB$_{321}$)$_2$ in living cells using smFRET-RAP*

We determined the dynamics of (MET:InlB$_{321}$)$_2$ dimers from an available single-molecule FRET data set recorded in living cells that was previously used to determine absolute FRET efficiencies for the dimeric complex [29]. Conceptually, two InlB$_{321}$ variants, each with a unique accessible cysteine at either position 64 (termed H for head) or position 280 (termed T for tail) (**Figure 1A**), were fluorescently labeled with either Cy3B or ATTO 647N (**Table S1**) [29]. Accessible volume simulation of the crystal structure of the (MET:InlB$_{321}$)$_2$ dimer [24] yielded expected FRET efficiencies between donor and acceptor of 0.620 (T-T), 0.567 (H-T/T-H), and 0.018 (H-H) [29]. Single-molecule FRET data in living cells were recorded using fluorescence bleaching and recovery (smFRET-RAP) [40] (**Figure 1B**). Using high-intensity excitation of both donor and acceptor fluorophores and TIRF illumination, fluorophore-labeled InlB$_{321}$ bound to MET at the basal membrane or adsorbed to the glass surface was photobleached. Following this, the cells were maintained in the dark to allow MET-bound InlB$_{321}$ to diffuse from the lateral and apical membranes back to the basal membrane, restoring a low-density signal that is suitable for single-molecule analysis. Next, smFRET video files were acquired using donor excitation and simultaneous detection of donor and acceptor fluorescence (see Methods). Only smFRET intensity traces showing anti-correlated intensity of donor and acceptor emission and one-step photobleaching were accepted for FRET efficiency calculations (**Figure S1**). Distinct populations with FRET efficiencies of 0.90 ± 0.05 for the T-T pair and 0.55 ± 0.09 for the H-T pair were found (**Figure 1C**), in good agreement with data obtained from fixed cells [29], yet broader FRET efficiency distributions were observed (**Figure S2A**).

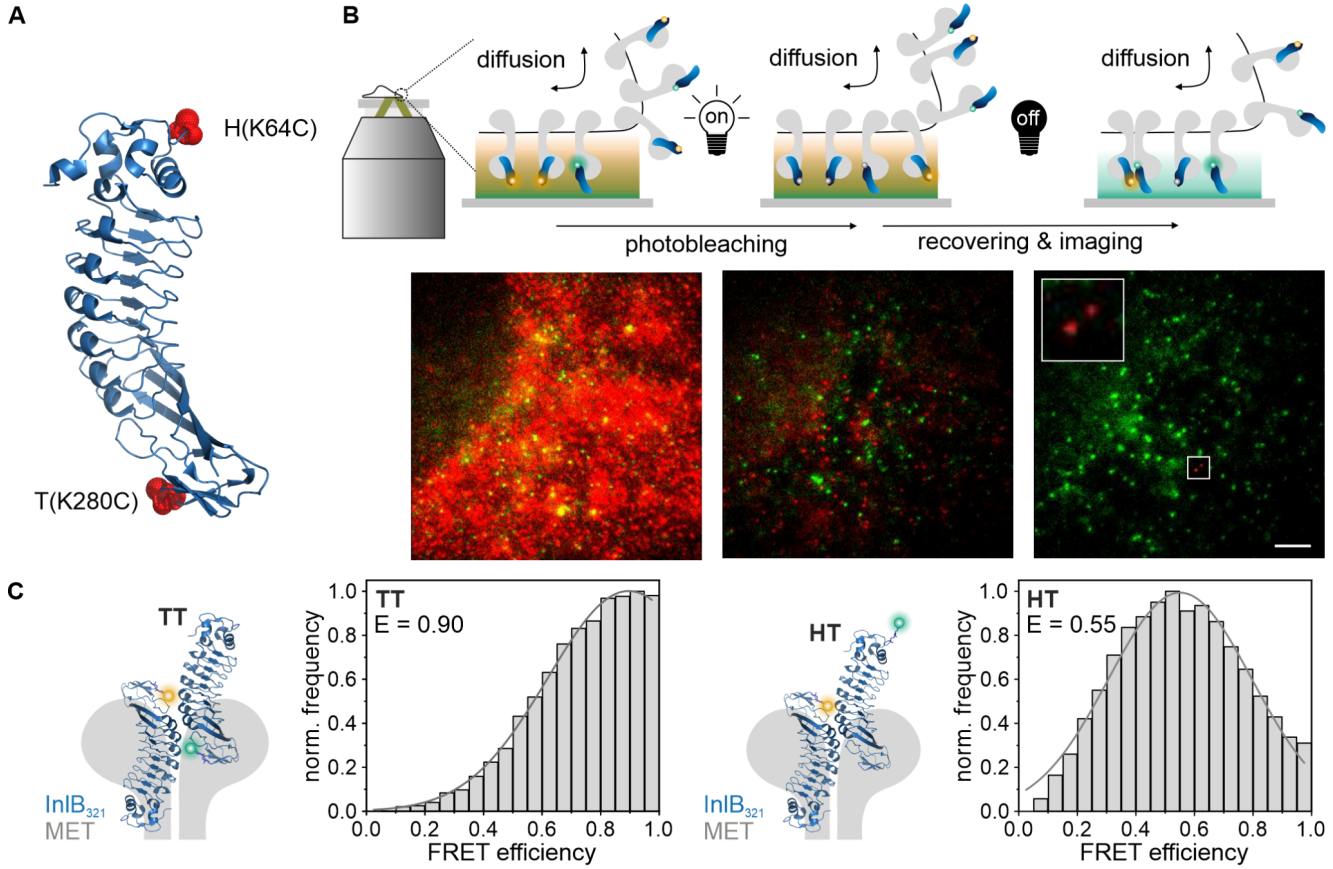


**Figure 1: smFRET-RAP experiments of (MET:InlB)$_2$ dimers in living cells. A**) crystal structure of InlB$_{321}$ (PDB 1H6T). The H (K64C) and T (K280C) mutations are highlighted in red. The two variants were labeled with either Cy3B or ATTO 647N, respectively. **B**) Schematic of smFRET-RAP (top) with example image before and after photobleaching, and during the single-molecule FRET measurement (bottom). Scale bar 5 µm. **C**) Live-cell smFRET efficiencies of (MET:InlB$_{321}$)$_2$ dimers labeled with Cy3B-T-InlB$_{321}$ and ATTO 647N-T-InlB$_{321}$ (left) or with Cy3B-H-InlB$_{321}$ and ATTO 647N-T-InlB$_{321}$ (right). The crystal structure of InlB is adapted from PDB: 2UZY.

*smFRET reports the lifetime of the dimeric (MET:InlB)$_2$ complex in living cells*

To determine the lifetime (association time) of dimeric (MET:InlB)$_2$ complexes in living cells, we reconstructed single-molecule trajectories and measured the duration of the FRET signal in these trajectories. First, a single-molecule FRET event is identified at the moment a signal in the acceptor emission channel is observed upon donor excitation (**Figure 2A**). Next, the single-molecule FRET signal is followed over time and a trajectory is reconstructed, including donor and acceptor fluorescence signals until both signals disappear (**Figure 2B; SI Movies 1-4**). The temporal length of the FRET segment of the trajectory was used to calculate the apparent lifetime of the dimeric (MET:InlB)$_2$ complex and was found to be 1.13 ± 0.06 s (T-T) and 0.80 ± 0.03 s (H-T) for the two FRET pairs, respectively (**Figure 2C**). In order to assess whether photobleaching is the major determinant of the trajectory length, we analyzed single-molecule FRET data of (MET:InlB)$_2$ complexes in fixed cells. The total lifetime of single-molecule FRET was found to be about 15-fold longer than in living cells (**Figure S2B**), indicating that the FRET lifetime in living cells is mainly dominated by the lifetime of the (MET:InlB)$_2$ complex. Furthermore, we observed that in about 30% of all FRET trajectories, the donor fluorescence emission persists after the acceptor signal disappears (**Figure S3A, E**).

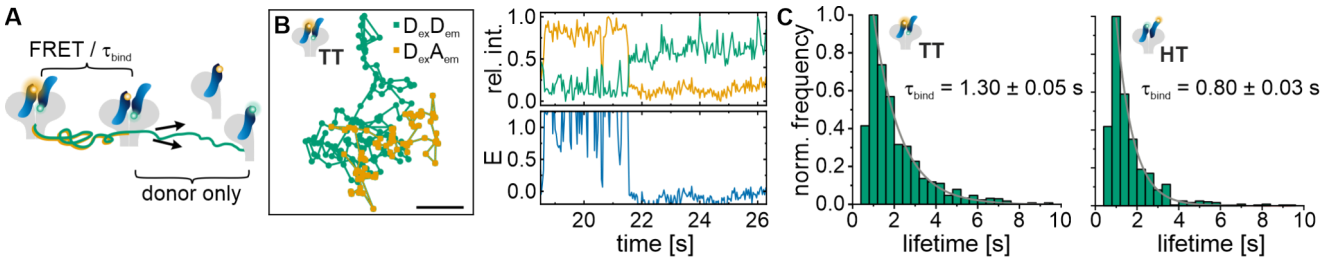


**Figure 2: Lifetime of the (MET:InlB)$_2$ dimer. A**) Scheme of a live-cell smFRET trajectory. The detection of a FRET signal is the starting point for a single-molecule trajectory, which is then recorded until both the donor and the acceptor are photobleached. **B**) Exemplary smFRET trajectory. The left panel shows the positions of the acceptor and donor, respectively, during FRET (orange) and after the acceptor signal disappeared (green). In the right panels, the corresponding intensities (donor in green, acceptor in orange) and FRET efficiencies over time are shown. Scale bar 500 nm. **C**) Histograms of the duration of the FRET segments in single-molecule trajectory deliver (MET:InlB)$_2$ dimer lifetimes for InlB T-T and H-T variants. The histograms were fitted with a single exponential decay. N = 27 cells (T-T) and 24 cells (H-T), 3 independent experiments.

*Diffusion properties of the dimeric (MET:InlB)$_2$ and monomeric (MET:InlB) are distinct*

Next, the diffusion coefficients and types were extracted from single-particle trajectories exhibiting FRET. Both segments of the trajectories were analyzed separately, the first one where FRET was detected, and the second one that followed the loss of acceptor signal and showed donor fluorescence only (**Figure 3**). For MET labeled with InlB T–T variants, the mean diffusion coefficient of FRET segments was 0.066 ± 0.044 μm$^2$/s, while donor-only segments exhibited a higher mean diffusion coefficient of 0.109 ± 0.068 μm$^2$/s. In cells where the MET receptor was labelled with H–T variants, the mean diffusion coefficients were 0.056 ± 0.038 μm$^2$/s for FRET trajectories and 0.093 ± 0.053 μm$^2$/s for donor-only trajectories. The distribution of diffusion coefficients showed a clear separation between FRET and donor-only segments, with the latter consistently displaying higher mobility (**Figure 3A**). Analysis of the types of motion revealed that 44% (T-T) and 50% (H-T) of FRET trajectories were classified as restricted diffusion, while the remaining 56% (T-T) and 50% (H-T) showed free diffusion. In contrast, in the donor-only segments, a smaller proportion (39% (T–T) and 33% (H–T)) showed restricted diffusion, whereas 61% (T-T) and 67% (H-T) showed free diffusion (**Figure 3B**). The analysis of the jump angle in the two segments of single-molecule trajectories showed a confined pattern for the FRET segment as compared to a random walk pattern for the donor-only segment (**Figure 3C**). We also examined the diffusion coefficient and mode of MET dimers for trajectories that began with a FRET signal and transitioned to a donor-only

signal after the acceptor signal disappeared (pathway 1) as compared to those that showed a loss in FRET signal without remaining donor-only signal (pathway 2) (**Figure S3**). While the diffusion coefficient of the FRET segment was found to be similar in both pathways (0.066 ± 0.044 $\mu m^2/s$ and 0.060 0.043 $\mu m^2/s$ in T-T labeled cells; 0.056 ± 0.038 $\mu m^2/s$ and 0.055 ± 0.040 $\mu m^2/s$ in H-T labeled cells) (**Figure S3B**), an increase in the fraction with restricted diffusion was observed (from 44% (pathway 1) to 60% (pathway 2) for T-T labelled cells, and from 50% (pathway 1) to 59% (pathway 2) in H–T labelled cells) (**Figure S3C**). The jump angle distribution for these segments of trajectories showed a similarly restricted motion (**Figure S3D**).

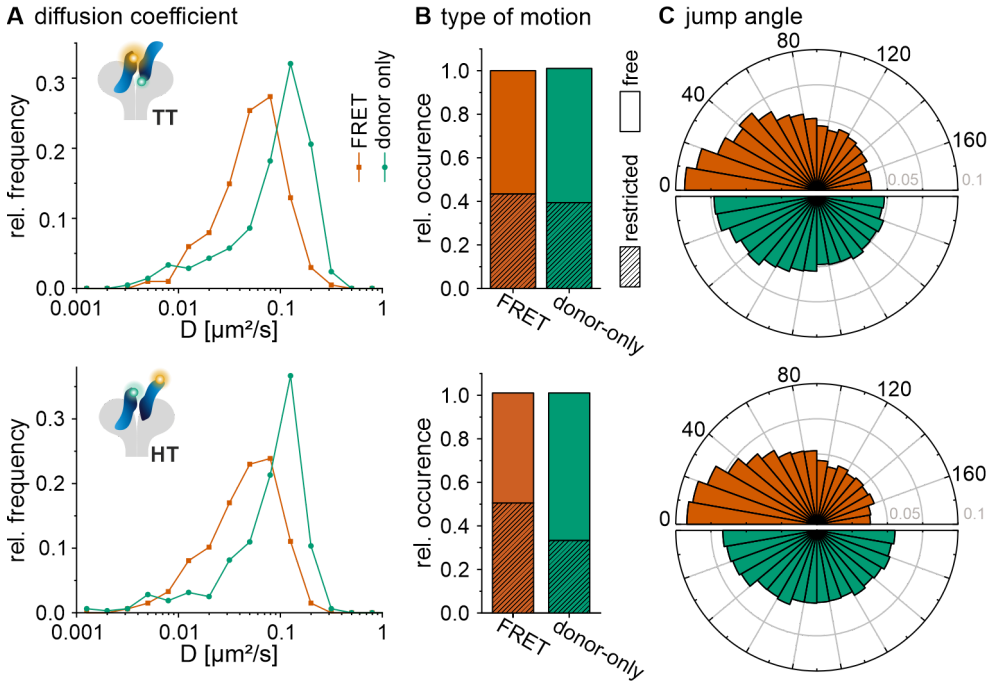


**Figure 3: Diffusion dynamics of MET:InlB extracted from FRET trajectories. A**) Distribution of diffusion coefficients for the FRET segment (orange) and the donor-only segment (green) of single-molecule trajectories (N = 27 cells, 24 cells measured with InlB T-T variants and H-T variants, respectively, from at least 3 independent experiments). **B**) Relative occurrence of restricted and free diffusion MET:InlB within FRET and donor-only segments of single-molecule trajectories. **C**) Distribution of jump angles within FRET and donor-only segments of single-molecule trajectories (grey circles represent relative frequencies).

## Discussion

The probability of detecting a single-molecule FRET event depends on the degree of labeling. For high protein expression levels, as observed for MET in many relevant cell lines [29], stoichiometric labeling may, however, preclude single-molecule detection. SPT in particular demands molecular densities smaller than the diffraction limit, ideally below 0.5 receptors/$\mu m^2$ [45]. To overcome these challenges, smFRET combined with fluorescence recovery after photobleaching (RAP) has proven particularly effective for studying native membrane receptors [40]. RAP minimizes signal overlap and background fluorescence, improving the specificity of single-molecule detection while maintaining a high labeling efficiency. We combined smFRET-RAP with single-particle tracking to detect dimer–monomer transitions of MET receptors in living cells and with single-molecule resolution. In addition, smFRET-RAP reduces fluorescence resulting from fluorophore-labeled ligands nonspecifically adsorbed to the surface. For instance, the hydrophobic ATTO 647N fluorophore used in this study is known to show increased surface binding, which in the SPT analysis appears as an immobile fraction and leads to an underestimation of diffusion coefficients [46, 47]. These artifacts were minimized by initial photobleaching in the smFRET-RAP workflow before the measurement. In addition, selecting only FRET trajectories with anti-correlated donor and acceptor signals ensures high specificity in the analyzed single-molecule

trajectories. Consistently, global mean squared displacement (MSD) analysis of FRET-positive trajectories revealed negligible immobile diffusion, validating the robustness of the approach.

The distributions of FRET efficiencies of the $(MET:InlB_{321})_2$ dimer recorded in living cells were broader than those in fixed cells (**Figure 1C, S2A**). Several parameters contribute to this observation: first, single-particle tracking in living cells requires shorter integration times to reliably capture the mobility of single molecules in the cell membrane [45, 48, 49]. Related to this, lower laser intensities were used in live-cell experiments to minimize phototoxicity, which in turn impacts signal-to-noise and signal-to-background values. Second, background intensities in live-cell experiments may be different and vary during an experiment. Lastly, it is possible that the $(MET:InlB_{321})_2$ complex exhibits some degree of structural flexibility in living cells, which, however, is beyond the current accuracy of the method.

The combination of single-molecule FRET and single-particle tracking allows for a segmentation of single-molecule trajectories, and thus a separate analysis of differently built molecular complexes. Single-molecule FRET trajectories of the $(MET:InlB_{321})_2$ dimer showed a loss in acceptor fluorescence after an average of 1.3 (InlB T-T) or 0.8 (InlB H-T) seconds (**Figure 2C**), whereas smFRET experiments in fixed cells showed a much longer duration of the FRET signal (of 19 and 13 seconds, respectively). This indicates that the duration of the FRET signal in live-cell experiments is predominantly determined by the lifetime of the $(MET:InlB_{321})_2$ dimer, and not influenced by photobleaching of the acceptor fluorophore. The loss in acceptor fluorescence in live-cell experiments can be further classified into two reaction pathways: continuous donor fluorescence in the single-molecule trajectory indicates at the dissociation of the $(MET:InlB_{321})_2$ dimer, whereas the simultaneous disappearance of both the donor and acceptor signals indicates that the dimeric complex moved beyond the TIRF detection limit [40, 50], possibly through cellular uptake such as e.g. endocytosis [15, 51]. Other explanations are possible, such as the off-dissociation of InlB ligands from the dimeric complex, yet are not accessible from the experimental data.

The determined lifetime of the $(MET:InlB_{321})_2$ dimer is similar to previously reported values for EGFR:EGF dimers [52–54]. Using a similar fluorophore-based labeling approach, Coban et al. reported an $(EGFR:EGF)_2$ complex lifetime of approximately 0.84 s in the breast cancer cell line HCC1054 [52]. Another study that employed quantum dot (QD)-labeled EGF in combination with hidden Markov modeling revealed longer lifetimes of EGFR:EGF dimers and a variation across different cell lines, with 3.59 s in the epidermoid carcinoma cell line A431, 13.02 s in HeLa cells, and 8.33 s in EGFR-transfected CHO cells [53, 54]. The longer lifetimes might be related to the larger QD labels, which exhibit outstanding brightness yet might also impede receptor mobility and subsequent processing steps of ligand-activated receptors. Notably, the diffusion coefficient of EGFR:EGF varied from 0.07 $\mu m^2/s$ with eGFP labeling to 0.014 $\mu m^2/s$ with QD labeling in CHO cells [54, 55].

From segmented trajectories, we observed a reduced diffusion coefficient of the dimeric $(MET:InlB)_2$ complex in the FRET segment as compared to the monomeric (dissociated) MET:InlB complex from the donor-only segment (**Figure 3**). Previous SPT studies have reported a reduction of the global diffusion coefficients of RTKs, including MET, upon ligand stimulation [30, 48, 49, 56–58]. In this work, we report the measurement of diffusion coefficients of the same receptor-ligand complex for two distinct molecular stoichiometries.

An alternative technology to investigate protein-protein interactions in the plasma membrane of living cells is two-color single-particle tracking (2cSPT) [45, 53, 59–64]. In 2cSPT experiments, dimers are identified by assigning two particles in two spectrally separate channels as co-localized if the distance is below a defined value [45, 59, 63–65]. The upper threshold for this distance threshold is determined by the localization precision of each channel and the accuracy of channel alignment [59]. However, in studies involving RTKs, which are mainly internalized through clathrin-mediated endocytosis (CME) [16, 66, 67], it is challenging to discriminate between RTK dimers and RTKs colocalized within clathrin-coated pits that exhibit a size from 70 to 150 nm and persist more than tens of seconds [68–71]. In contrast,

smFRET in living cells offers an elegant alternative to detect *bona fide* receptor dimers, given the short range of the FRET interaction of less than 10 nm and the feature of anti-correlated donor and acceptor intensity traces [40, 45, 65].

Following ligand binding and receptor dimerization, intracellular signaling is initiated by adaptor protein recruitment, such as Grb2 binding to ligand-activated MET. Previous studies reported that Grb2 binds to activated EGFR with a lifetime of approximately 0.13 s in both *in vivo* and *in vitro* systems [72, 73]. Within this context, the ~1-second lifetime of $(MET:InlB)_2$ dimers seems plausible. Following signaling initiation, RTKs may also be recycled through CME, a key regulatory mechanism for RTK downregulation. CME involves an initial approximately 10 second phase for clathrin-coated pit formation, followed by membrane invagination and vesicle internalization over the course of 20 seconds to several minutes [69, 70].

In summary, the presented experimental approach presents a robust method to measure the stability of ligand-activated membrane receptors in living cells, and to assess the diffusion properties of differently constituted receptor complexes. The approach is transferable to other membrane proteins, and it can serve as a platform to assess how modifications in proteins or the addition of modulators alter the stability of receptor dimers.

## Author contributions

MH and YL designed the research. HHN designed the FRET study and provided labeled proteins. YL performed live-cell single-molecule imaging experiments and image analysis with support from MSD. HDB built the optical setup for smFRET. YL, HHN, MSD, and MH discussed the data and wrote the manuscript.

## Funding

MH, MSD, and YL acknowledge funding by the Deutsche Forschungsgemeinschaft (DFG) (grant SFB 1507).

## Acknowledgments

We are grateful to Inga Hänelt and Roberto Covino for helpful discussions. We thank Petra Freund for support with cell culture and Wenjun Wang for assistance with coding.

## Data availability

The data is available in the EMBL BioImaging Archive under accession code S-BIAD1347 (https://www.ebi.ac.uk/biostudies/bioimages/studies/S-BIAD1347). Custom-written software used in this work was written in Python and MatLab and is available from the authors upon request.

## Conflict of interest

The authors declare no conflict of interest.

## References

1. Trusolino L, Bertotti A, Comoglio PM (2010) MET signalling: principles and functions in development, organ regeneration and cancer. Nat Rev Mol Cell Biol 11:834–848. https://doi.org/10.1038/nrm3012

2. Petrini I (2015) Biology of MET: a double life between normal tissue repair and tumor progression. Ann Transl Med 3:82. https://doi.org/10.3978/j.issn.2305-5839.2015.03.58

3. Birchmeier C, Birchmeier W, Gherardi E, Vande Woude GF (2003) Met, metastasis, motility and

more. Nat Rev Mol Cell Biol 4:915–925. https://doi.org/10.1038/nrm1261

4. Koch JP, Aebersold DM, Zimmer Y, Medová M (2020) MET targeting: time for a rematch. Oncogene 39:2845–2862. https://doi.org/10.1038/s41388-020-1193-8

5. Mellado-Gil J, Rosa TC, Demirci C, et al (2011) Disruption of hepatocyte growth factor/c-Met signaling enhances pancreatic beta-cell death and accelerates the onset of diabetes. Diabetes 60:525–536. https://doi.org/10.2337/db09-1305

6. Campbell DB, Sutcliffe JS, Ebert PJ, et al (2006) A genetic variant that disrupts MET transcription is associated with autism. Proc Natl Acad Sci U S A 103:16834–16839. https://doi.org/10.1073/pnas.0605296103

7. Stoker M, Gherardi E, Perryman M, Gray J (1987) Scatter factor is a fibroblast-derived modulator of epithelial cell mobility. Nature 327:239–242. https://doi.org/10.1038/327239a0

8. Nakamura T, Nishizawa T, Hagiya M, et al (1989) Molecular cloning and expression of human hepatocyte growth factor. Nature 342:440–443. https://doi.org/10.1038/342440a0

9. Gherardi E, Youles ME, Miguel RN, et al (2003) Functional map and domain structure of MET, the product of the c-met protooncogene and receptor for hepatocyte growth factor/scatter factor. Proc Natl Acad Sci U S A 100:12039–12044. https://doi.org/10.1073/pnas.2034936100

10. Uchikawa E, Chen Z, Xiao G-Y, et al (2021) Structural basis of the activation of c-MET receptor. Nat Commun 12:4074. https://doi.org/10.1038/s41467-021-24367-3

11. Banerjee M, Copp J, Vuga D, et al (2004) GW domains of the Listeria monocytogenes invasion protein InlB are required for potentiation of Met activation. Mol Microbiol 52:257–271. https://doi.org/10.1111/j.1365-2958.2003.03968.x

12. Shen Y, Naujokas M, Park M, Ireton K (2000) InIB-dependent internalization of Listeria is mediated by the Met receptor tyrosine kinase. Cell 103:501–510. https://doi.org/10.1016/s0092-8674(00)00141-0

13. Lemmon MA, Schlessinger J (2010) Cell signaling by receptor tyrosine kinases. Cell 141:1117–1134. https://doi.org/10.1016/j.cell.2010.06.011

14. Jeffers M, Taylor GA, Weidner KM, et al (1997) Degradation of the Met tyrosine kinase receptor by the ubiquitin-proteasome pathway. Mol Cell Biol 17:799–808. https://doi.org/10.1128/MCB.17.2.799

15. Hammond DE, Urbé S, Vande Woude GF, Clague MJ (2001) Down-regulation of MET, the receptor for hepatocyte growth factor. Oncogene 20:2761–2770. https://doi.org/10.1038/sj.onc.1204475

16. von Zastrow M, Sorkin A (2021) Mechanisms for Regulating and Organizing Receptor Signaling by Endocytosis. Annu Rev Biochem 90:709–737. https://doi.org/10.1146/annurev-biochem-081820-092427

17. Veiga E, Cossart P (2005) Listeria hijacks the clathrin-dependent endocytic machinery to invade mammalian cells. Nat Cell Biol 7:894–900. https://doi.org/10.1038/ncb1292

18. Gaillard JL, Berche P, Frehel C, et al (1991) Entry of L. monocytogenes into cells is mediated by internalin, a repeat protein reminiscent of surface antigens from gram-positive cocci. Cell 65:1127–1141. https://doi.org/10.1016/0092-8674(91)90009-n

19. Hamon M, Bierne H, Cossart P (2006) Listeria monocytogenes: a multifaceted model. Nat Rev Microbiol 4:423–434. https://doi.org/10.1038/nrmicro1413

20. Braun L, Ohayon H, Cossart P (1998) The InIB protein of Listeria monocytogenes is sufficient to promote entry into mammalian cells. Mol Microbiol 27:1077–1087.

https://doi.org/10.1046/j.1365-2958.1998.00750.x

21. Parida SK, Domann E, Rohde M, et al (1998) Internalin B is essential for adhesion and mediates the invasion of Listeria monocytogenes into human endothelial cells. Mol Microbiol 28:81–93. https://doi.org/10.1046/j.1365-2958.1998.00776.x

22. Ireton K, Payrastre B, Chap H, et al (1996) A role for phosphoinositide 3-kinase in bacterial invasion. Science 274:780–782. https://doi.org/10.1126/science.274.5288.780

23. Li N, Xiang G-S, Dokainish H, et al (2005) The Listeria protein internalin B mimics hepatocyte growth factor-induced receptor trafficking. Traffic 6:459–473. https://doi.org/10.1111/j.1600-0854.2005.00290.x

24. Niemann HH, Jäger V, Butler PJG, et al (2007) Structure of the human receptor tyrosine kinase met in complex with the Listeria invasion protein InlB. Cell 130:235–246. https://doi.org/10.1016/j.cell.2007.05.037

25. Baldering TN, Karathanasis C, Harwardt M-LIE, et al (2021) CRISPR/Cas12a-mediated labeling of MET receptor enables quantitative single-molecule imaging of endogenous protein organization and dynamics. iScience 24:101895. https://doi.org/10.1016/j.isci.2020.101895

26. Dietz MS, Haße D, Ferraris DM, et al (2013) Single-molecule photobleaching reveals increased MET receptor dimerization upon ligand binding in intact cells. BMC Biophys 6:6. https://doi.org/10.1186/2046-1682-6-6

27. Niemann HH, Gherardi E, Bleymüller WM, Heinz DW (2012) Engineered variants of InlB with an additional leucine-rich repeat discriminate between physiologically relevant and packing contacts in crystal structures of the InlB:MET complex. Protein Sci 21:1528–1539. https://doi.org/10.1002/pro.2142

28. Ferraris DM, Gherardi E, Di Y, et al (2010) Ligand-mediated dimerization of the Met receptor tyrosine kinase by the bacterial invasion protein InlB. J Mol Biol 395:522–532. https://doi.org/10.1016/j.jmb.2009.10.074

29. Li Y, Arghittu SM, Dietz MS, et al (2024) Single-molecule imaging and molecular dynamics simulations reveal early activation of the MET receptor in cells. Nat Commun 15:9486. https://doi.org/10.1038/s41467-024-53772-7

30. Harwardt M-LIE, Young P, Bleymüller WM, et al (2017) Membrane dynamics of resting and internalin B-bound MET receptor tyrosine kinase studied by single-molecule tracking. FEBS Open Bio 7:1422–1440. https://doi.org/10.1002/2211-5463.12285

31. Bremer EG, Schlessinger J, Hakomori S (1986) Ganglioside-mediated modulation of cell growth. Specific effects of GM3 on tyrosine phosphorylation of the epidermal growth factor receptor. J Biol Chem 261:2434–2440

32. Coskun Ü, Grzybek M, Drechsel D, Simons K (2011) Regulation of human EGF receptor by lipids. Proc Natl Acad Sci U S A 108:9044–9048. https://doi.org/10.1073/pnas.1105666108

33. Andl CD, Rustgi AK (2005) No one-way street: cross-talk between e-cadherin and receptor tyrosine kinase (RTK) signaling: a mechanism to regulate RTK activity. Cancer Biol Ther 4:28–31. https://doi.org/10.4161/cbt.4.1.1431

34. Paul MD, Hristova K (2019) The RTK Interactome: Overview and Perspective on RTK Heterointeractions. Chem Rev 119:5881–5921. https://doi.org/10.1021/acs.chemrev.8b00467

35. Lin C-W, Nocka LM, Stinger BL, et al (2022) A two-component protein condensate of the EGFR cytoplasmic tail and Grb2 regulates Ras activation by SOS at the membrane. Proc Natl Acad Sci U S A 119:e2122531119. https://doi.org/10.1073/pnas.2122531119

36. Rohwedder A, Knipp S, Roberts LD, Ladbury JE (2021) Composition of receptor tyrosine kinase-mediated lipid micro-domains controlled by adaptor protein interaction. Sci Rep 11:6160. https://doi.org/10.1038/s41598-021-85578-8

37. Tomuleasa C, Tigu A-B, Munteanu R, et al (2024) Therapeutic advances of targeting receptor tyrosine kinases in cancer. Signal Transduct Target Ther 9:201. https://doi.org/10.1038/s41392-024-01899-w

38. Kiyatkin A, van Alderwerelt van Rosenburgh IK, Klein DE, Lemmon MA (2020) Kinetics of receptor tyrosine kinase activation define ERK signaling dynamics. Sci Signal 13.: https://doi.org/10.1126/scisignal.aaz5267

39. Wells A, Welsh JB, Lazar CS, et al (1990) Ligand-induced transformation by a noninternalizing epidermal growth factor receptor. Science 247:962–964. https://doi.org/10.1126/science.2305263

40. Asher WB, Geggier P, Holsey MD, et al (2021) Single-molecule FRET imaging of GPCR dimers in living cells. Nat Methods 18:397–405. https://doi.org/10.1038/s41592-021-01081-y

41. Edelstein AD, Tsuchida MA, Amodaj N, et al (2014) Advanced methods of microscope control using μManager software. J Biol Methods 1.: https://doi.org/10.14440/jbm.2014.36

42. Preus S, Noer SL, Hildebrandt LL, et al (2015) iSMS: single-molecule FRET microscopy software. Nat Methods 12:593–594. https://doi.org/10.1038/nmeth.3435

43. Jaqaman K, Loerke D, Mettlen M, et al (2008) Robust single-particle tracking in live-cell time-lapse sequences. Nat Methods 5:695–702. https://doi.org/10.1038/nmeth.1237

44. Juette MF, Terry DS, Wasserman MR, et al (2016) Single-molecule imaging of non-equilibrium molecular ensembles on the millisecond timescale. Nat Methods 13:341–344. https://doi.org/10.1038/nmeth.3769

45. Wilmes S, Hafer M, Vuorio J, et al (2020) Mechanism of homodimeric cytokine receptor activation and dysregulation by oncogenic mutations. Science 367:643–652. https://doi.org/10.1126/science.aaw3242

46. Zanetti-Domingues LC, Tynan CJ, Rolfe DJ, et al (2013) Hydrophobic fluorescent probes introduce artifacts into single molecule tracking experiments due to non-specific binding. PLoS One 8:e74200. https://doi.org/10.1371/journal.pone.0074200

47. Zanetti-Domingues LC, Martin-Fernandez ML, Needham SR, et al (2012) A systematic investigation of differential effects of cell culture substrates on the extent of artifacts in single-molecule tracking. PLoS One 7:e45655. https://doi.org/10.1371/journal.pone.0045655

48. Harwardt M-LIE, Schröder MS, Li Y, et al (2020) Single-Molecule Super-Resolution Microscopy Reveals Heteromeric Complexes of MET and EGFR upon Ligand Activation. Int J Mol Sci 21.: https://doi.org/10.3390/ijms21082803

49. Catapano C, Rahm JV, Omer M, et al (2023) Biased activation of the receptor tyrosine kinase HER2. Cell Mol Life Sci 80:158. https://doi.org/10.1007/s00018-023-04806-8

50. Toomre D, Bewersdorf J (2010) A new wave of cellular imaging. Annu Rev Cell Dev Biol 26:285–314. https://doi.org/10.1146/annurev-cellbio-100109-104048

51. Li N, Hill KS, Elferink LA (2008) Analysis of receptor tyrosine kinase internalization using flow cytometry. Methods Mol Biol 457:305–317. https://doi.org/10.1007/978-1-59745-261-8_23

52. Coban O, Zanetti-Dominguez LC, Matthews DR, et al (2015) Effect of phosphorylation on EGFR dimer stability probed by single-molecule dynamics and FRET/FLIM. Biophys J 108:1013–1026. https://doi.org/10.1016/j.bpj.2015.01.005

53. Low-Nam ST, Lidke KA, Cutler PJ, et al (2011) ErbB1 dimerization is promoted by domain co-confinement and stabilized by ligand binding. Nat Struct Mol Biol 18:1244–1249. https://doi.org/10.1038/nsmb.2135

54. Valley CC, Arndt-Jovin DJ, Karedla N, et al (2015) Enhanced dimerization drives ligand-independent activity of mutant epidermal growth factor receptor in lung cancer. Mol Biol Cell 26:4087–4099. https://doi.org/10.1091/mbc.E15-05-0269

55. Vámosi G, Friedländer-Brock E, Ibrahim SM, et al (2019) EGF Receptor Stalls upon Activation as Evidenced by Complementary Fluorescence Correlation Spectroscopy and Fluorescence Recovery after Photobleaching Measurements. Int J Mol Sci 20.: https://doi.org/10.3390/ijms20133370

56. Mudumbi KC, Burns EA, Schodt DJ, et al (2024) Distinct interactions stabilize EGFR dimers and higher-order oligomers in cell membranes. Cell Rep 43:113603. https://doi.org/10.1016/j.celrep.2023.113603

57. Marchetti L, Luin S, Bonsignore F, et al (2015) Ligand-induced dynamics of neurotrophin receptors investigated by single-molecule imaging approaches. Int J Mol Sci 16:1949–1979. https://doi.org/10.3390/ijms16011949

58. Catapano C, Dietz MS, Kompa J, et al (2025) Long-Term Single-Molecule Tracking in Living Cells using Weak-Affinity Protein Labeling. Angew Chem Int Ed Engl 64:e202413117. https://doi.org/10.1002/anie.202413117

59. Niederauer C, Nguyen C, Wang-Henderson M, et al (2023) Dual-color DNA-PAINT single-particle tracking enables extended studies of membrane protein interactions. Nat Commun 14:4345. https://doi.org/10.1038/s41467-023-40065-8

60. da Rocha-Azevedo B, Lee S, Dasgupta A, et al (2020) Heterogeneity in VEGF Receptor-2 Mobility and Organization on the Endothelial Cell Surface Leads to Diverse Models of Activation by VEGF. Cell Rep 32:108187. https://doi.org/10.1016/j.celrep.2020.108187

61. Kasai RS, Suzuki KGN, Prossnitz ER, et al (2011) Full characterization of GPCR monomer-dimer dynamic equilibrium by single molecule imaging. J Cell Biol 192:463–480. https://doi.org/10.1083/jcb.201009128

62. Wilmes S, Beutel O, Li Z, et al (2015) Receptor dimerization dynamics as a regulatory valve for plasticity of type I interferon signaling. J Cell Biol 209:579–593. https://doi.org/10.1083/jcb.201412049

63. Bai X, Sun P, Wang X, et al (2023) Structure and dynamics of the EGFR/HER2 heterodimer. Cell Discov 9:18. https://doi.org/10.1038/s41421-023-00523-5

64. Tsirigotaki A, Dansercoer A, Verschueren KHG, et al (2023) Mechanism of receptor assembly via the pleiotropic adipokine Leptin. Nat Struct Mol Biol 30:551–563. https://doi.org/10.1038/s41594-023-00941-9

65. Bellón JS, Birkholz O, Richter CP, et al (2022) Four-color single-molecule imaging with engineered tags resolves the molecular architecture of signaling complexes in the plasma membrane. Cell Reports Methods 2:100165. https://doi.org/10.1016/j.crmeth.2022.100165

66. Goh LK, Sorkin A (2013) Endocytosis of receptor tyrosine kinases. Cold Spring Harb Perspect Biol 5:a017459. https://doi.org/10.1101/cshperspect.a017459

67. Alfonzo-Méndez MA, Sochacki KA, Strub M-P, Taraska JW (2022) Dual clathrin and integrin signaling systems regulate growth factor receptor activation. Nat Commun 13:905. https://doi.org/10.1038/s41467-022-28373-x

68. Kirchhausen T, Owen D, Harrison SC (2014) Molecular structure, function, and dynamics of

clathrin-mediated membrane traffic. Cold Spring Harb Perspect Biol 6:a016725. https://doi.org/10.1101/cshperspect.a016725

69. Aguet F, Antonescu CN, Mettlen M, et al (2013) Advances in analysis of low signal-to-noise images link dynamin and AP2 to the functions of an endocytic checkpoint. Dev Cell 26:279–291. https://doi.org/10.1016/j.devcel.2013.06.019

70. Saffarian S, Cocucci E, Kirchhausen T (2009) Distinct dynamics of endocytic clathrin-coated pits and coated plaques. PLoS Biol 7:e1000191. https://doi.org/10.1371/journal.pbio.1000191

71. Mund M, Tschanz A, Wu Y-L, et al (2023) Clathrin coats partially preassemble and subsequently bend during endocytosis. J Cell Biol 222.: https://doi.org/10.1083/jcb.202206038

72. Yasui M, Hiroshima M, Kozuka J, et al (2018) Automated single-molecule imaging in living cells. Nat Commun 9:3061. https://doi.org/10.1038/s41467-018-05524-7

73. Morimatsu M, Takagi H, Ota KG, et al (2007) Multiple-state reactions between the epidermal growth factor receptor and Grb2 as observed by using single-molecule analysis. Proc Natl Acad Sci U S A 104:18013–18018. https://doi.org/10.1073/pnas.0701330104